Available online at www.sciencedirect.com
ScienceDirect
Trans. Nonferrous Met. Soc. China 35(2025) 207−224
Transactions of Nonferrous Metals Society of China
www.tnmsc.cn

Pyrimidine derivative as eco-friendly corrosion inhibitor for nickel−aluminum bronze in seawater

Jin-yu PI, Qi WANG, Chao-yang FU

Key Laboratory of Material Chemistry for Energy Conversion and Storage, Ministry of Education,
Hubei Key Laboratory of Materials Chemistry and Service Failure,
School of Chemistry and Chemical Engineering, Huazhong University of Science and Technology,
Wuhan 430074, China

Received 9 May 2023; accepted 15 November 2023

Abstract: A pyrimidine derivative, 6-phenyl-2-thiouracil (PT), was synthesized for developing a corrosion inhibitor (CI) applied in the protection of the nickel−aluminum bronze (NAB) in seawater. The anti-corrosion effect of PT was evaluated by the mass loss experiment, electrochemical tests and surface analysis. The results show that PT exhibits excellent inhibition performance and the maximum inhibition efficiency of PT reaches 99.6%. The interaction mechanism was investigated through X-ray photoelectron spectroscopy (XPS) and molecule dynamics simulation based on the density functional theory (DFT). The S—Cu, Al—N and Cu—N bonds are formed by the chemical interactions, leading to the adsorption of PT on the NAB surface. The diffusion of corrosive species is hindered considerably by the protective PT film with composition of $(\text{PT—Cu})_{\text{ads}}$ and $(\text{PT—Al})_{\text{ads}}$ on the PT/NAB interface. The degree of suppression is increased with the addition of more PT molecules.

Key words: nickel−aluminum bronze; corrosion inhibitor; diffusion coefficient; adsorption; seawater

1 Introduction

The nickel−aluminum bronze (NAB), a kind of aluminum bronzes with some other alloying elements (Fe, Mn, Ni, etc.), is the most extensively exploited in marine systems, exhibiting a range of beneficial properties in seawater [1−5]. Unfortunately, the problems of severe corrosion phenomenon such as pitting and crevice are inescapable under long exposure to the harming medium [6−8]. The cost of the anti-corrosion engineering of NAB such as heat treatment and surface modifications every year is countless [9−12]. Accordingly, a lower and easier method of adding corrosion inhibitors (CI) into the medium can be applied in advancing the performance of the corrosion shield [13].

Numerous studies denote that organic molecules containing active groups or heteroatoms are frequently used for the corrosion mitigation of copper and copper alloys [14−16]. Nitrogenous heterocyclic CIs can usually interact with copper and its alloy by the adsorption behavior between heteroatoms such as S, N, O, P atoms and the metal substrate [17,18]. Heteroatom-based CIs exhibit tremendous potential for anti-corrosion applications of NAB [19].

Traditional organic CIs with poisonous and costly properties are not consonant with vision of eco-friendly society [20]. Meanwhile, the preserve of ocean environment has become essential problem [21]. Thus, in recent years, the development of organic CIs with high performance

---

Corresponding author: Chao-yang FU, Tel: +86-13871507019, E-mail: cyfu@hust.edu.cn

https://doi.org/10.1016/S1003-6326(24)66675-6

and environmental friendliness displays a major trend in the field of metal corrosion protection [22,23]. Pyrimidine and its derivatives containing N-heterocyclic have been proven to be a diverse array of biological and pharmacological activities including anticonvulsant, antibacterial, antifungal, antiviral and anticancer properties, which suggests their huge potential to be eco-friendly CIs [24,25]. Besides, pyrimidine derivatives, as pharmaceutical intermediates, can be naturally degraded in seawater and are harmless to organisms. In fact, many studies have proven that pyrimidine derivatives, as a nitrogenous organic compound, can add some polar groups such as —SH, —OH, —NH_2, benzene rings, etc. to the pyrimidine ring to improve the adsorption capacity of the CI. Consequently, the CIs pertain to organics with 2-mercaptopyrimidine rings as the main structure are potential to become excellent and eco-friendly seawater CIs [26,27]. However, many studies are inclined to the exploitation of CIs on carbon steel and copper, and in addition to huge shortfall in the investigation on the development of CIs on NAB, the corresponding inhibition mechanism of CIs on NAB is also not comprehensive. For the applied environment, most pyrimidine inhibitors are usually applied in acidic medium while seldom in neutral seawater for copper material [28−30].

In this study, a pyrimidine inhibitor has been used for the first time in the anti-corrosion of NAB in seawater. 6-phenyl-2-thiouracil (PT) can be obtained by a one-step synthesis method at room temperature. The corrosion inhibition effect of PT in seawater has also been evaluated by mass loss experiment, electrochemical test and surface analysis. The 30 d mass loss progression of NAB has been elucidated through the application of a first-order kinetic model. The calculated diffusion coefficients (D_i) of H_2O with different concentrations of PT can deepen the link between theoretical calculation and experiment. Combined with the results of XPS, energy dispersive spectrometer (EDS) and theoretical calculations based on DFT and molecular dynamics simulation, the interaction mechanism and diffusion behavior of corrosive species on the NAB/PT/solution interface have been investigated in more in-depth level. The synthesis method adopted in this study is simple to operate, and the synthetic raw materials are environmentally friendly, green and harmless, which provides a new idea for the development of green corrosion CIs.

2 Experimental

2.1 Materials

The ingredient compositions of the NAB samples and the corrosive medium applied in the experiments are given in Tables 1 and 2. The chemical reagents including ethyl benzoylacetate (Macklin, 98%) and thiourea (Macklin, 98%) are all in analytical purity.

2.2 Synthesis of PT

As shown as Fig. 1, a similar synthesis method reported in the literature was used in this work [31].

Table 1 Ingredient compositions of NAB samples (wt.%)

Sn	Zn	Pb	P	Al	Fe	Mn	Si	Others	Cu
<0.1	<1.0	<0.01	<0.01	8.0−10.0	2.0−4.0	<0.5	<0.1	<1.7	Bal.

Table 2 Compositions of seawater used as corrosive medium (g/L)

NaCl	$MgCl_2$	Na_2SO_4	$CaCl_2$	KCl	$NaHCO_3$	KBr	H_3BO_3
24.5	5.20	4.09	1.16	0.201	0.101	0.101	0.0270

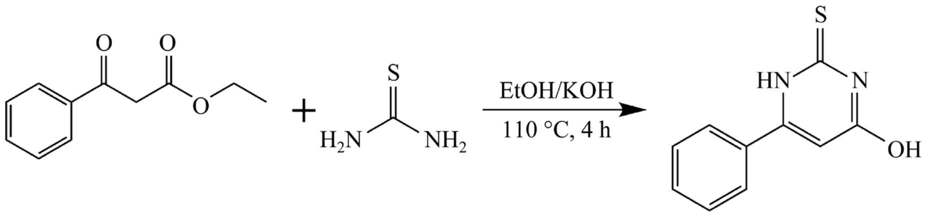

Fig. 1 Synthetic route of 6-phenyl-2-thiouracil (PT)

A mixture of KOH (1.9 g), thiourea (2.6 g) and 3 mL of benzoylacetate were added into ethanol (45 mL). The mixture was then heated and stirred for 4−5 h. The white solid product obtained by the amination reaction was further purified with hydrochloric acid. The lightly yellow crystal product was obtained by cooling crystallization and vacuum pressure filtration. Finally, the product was dried in a vacuum oven and PT was obtained after 24 h (yield of 56%).

^{1}H NMR analysis was used to characterize the structure of PT: ^{1}H NMR (400 MHz, DMSO-d6) δ 10.66 (s, 1H, NH), 8.20−7.67 (m, 2H, HAr), 7.61−7.06 (m, 3H, HAr), 6.06 (d, J=1.8 Hz, 1H, CH) (Fig. S1 in Supporting Information). Mass spectrometry as an extremely precise analysis method was performed using ESI-TOF mass spectrometer to obtain the relative molecular mass of PT [32]. Figure 2 shows the mass spectrum of PT. The fragment ions play an important role in the definition of the relative molecular mass of organic compounds. $[PT+K]^+$ was formed resulting from the pollution of analytical instrument [32]. The extremely low difference of the two value (0.0007 g/mol) indicated the successful synthesis of PT.

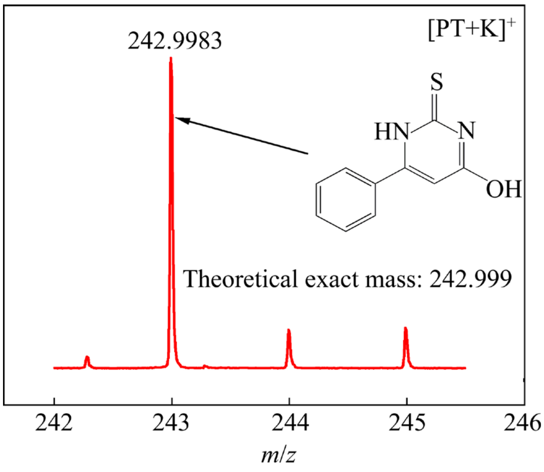

Fig. 2 Mass spectrum of 6-phenyl-2-thiouracil (PT)

2.3 Mass loss experiment

The NAB alloys for the mass loss experiment were cut into cubic of 5.0 cm × 1.0 cm × 0.3 cm following the abrasion with 600$^{\#}$, 800$^{\#}$, 1000$^{\#}$ and 1200$^{\#}$ sandpapers. The abrased NAB samples were successively washed with ethanol and deionized water. The immersion time was set as 6, 12, 18, 24 and 30 d. The mass loss (Δm) is the average of the three NAB specimens. The average corrosion rate ($V_{\rm corr}$) and the IE ($\eta_{\rm w}$, %) can be calculated on account of Eqs. (1)−(3) [33,34]:

$$\Delta m=\frac{w_1-w_2}{S} \tag{1}$$

$$V_{\rm corr}=\frac{w_1-w_2}{St} \tag{2}$$

$$\eta_w=\frac{v_1-v_2}{v_1}\times 100\% \tag{3}$$

where S is the total area of NAB samples, t is the immersion corrosion time, w_1 is the initial mass, w_2 is the residual mass, and v_1 and v_2 are the corrosion rates of the blank and with PT.

2.4 Electrochemical measurements

The traditional three-electrode test systems, including working electrodes, a saturated calomel electrode (SCE) and Pt electrode, were investigated by electrochemical testing. The NAB electrode was embedded in an epoxy adhesive. NAB specimens were exposed to the corrosive medium in an area of 1 cm × 1 cm. When the OCP approached a constant, EIS tests with frequencies set from 10^5 to 10^{-2} Hz were performed. Corrosion potential ($\varphi_{\rm corr}$), corrosion current density ($J_{\rm corr}$), Tafel slope including anode ($\beta_{\rm a}$) and Cathodic ($\beta_{\rm c}$) were obtained from the Tafel curve. The scanning rate was 1 mV/s with potential regions of OCP−200 mV to OCP + 200 mV. Three parallel experiments were conducted.

2.5 Surface analysis

For SEM (Quanta 200), XPS (AXIS-ULTRA DLD-600W) and water contact angle (WCA) test (Datapphysics), NAB samples were abraded with sandpaper of different roughness (600$^{\#}$−1200$^{\#}$). Subsequently, the samples were placed in corrosive media without and with 1.36 mmol/L PT. The immersion time for SEM, XPS and water contact angle (WCA) tests was 48, 48 and 6 h, respectively. After immersion, the sample was dried with nitrogen. For AFM, NAB metal needed to be polished with a polishing cloth accompanied by a polishing agent.

2.6 Calculation method

Some quantum chemistry parameters of PT structure including the highest occupied orbital energy ($E_{\rm HOMO}$), the lowest unoccupied molecular orbital energy (E_{LUMO}), dipole moment (μ), electronegativity (χ) and global hardness (η) were taken into account by gaussian 16 W based on density functional theory (DFT) method at RB3LYP-6-311G(d) level. Molecular electrostatic potential (MEP) of geometrically optimized PT was visualized through VMD [35] and Multiwfn [36].

The molecular dynamics (MD) simulation was carried out to theoretically probe the adsorption of PT through Material Studio 2020. Since the energy of $CuAl_3$ (110) surface was the lowest, a $CuAl_3$ (110) slab was cleaved to conduct a 3D periodic model with a 5×5 super cell. The solution box simulating seawater environment contained 1000 water molecules, 10 Na^+ atoms, 10 Cl^- atoms and one molecular of PT. The NAB-solution interface was composed of a periodic multislab, the solution box and a vacuum spacing of 10 Å to account for spurious interactions between slabs. Before the simulation calculation, the atoms of remaining 9 layers except for the top layer were frozen in fixed cartesian positions. The MD simulation was conducted via Forcite module in COMPASS II force field, set at 303 K, 1 fs time step and a simulation time of 500 ps in a NVT canonical ensemble.

The MD simulation was also used to theoretically explore the anti-corrosion effect of PT on the diffusion behavior of water molecules and the aggressive species (Cl^-, Cu^{2+}, Cu^+, O_2 and OH^-). All diffusion models contained the NAB substrate ($CuAl_3$) and solution layer with a 15 Å vacuum for the purpose of simulating more authentic NAB/PT/solution interface. Different solution simulation boxes were created, named A, B, C, D and E. All of them included 500 H_2O, 3 Cu^{2+}, 3 Cu^+, 3 O_2, 3 OH^- and 6 Cl^- molecules enabling the simulation boxes to maintain an electrically neutral state. The numbers of PT molecules for A, B, C, D, E were 0, 15, 30, 45 and 60, respectively. The diffusion coefficients (D_i) are determined by the mean squared displacement (MSD) analysis, which is expressed as follows [37,38]:

$$D_i = \frac{1}{6N}\lim_{t\to\infty}\frac{\mathrm{d}}{\mathrm{d}t}\sum_{i=1}^{N}|\boldsymbol{r}_i(t)-\boldsymbol{r}_i(0)|^2 \qquad (4)$$

where N the number of molecules, and $r_i(t)$ and $r_i(0)$ are the position vectors at time t and the initial moment.

3 Results and discussion

3.1 Mass loss experiment results

Mass loss experiments have been conducted to evaluate the anti-corrosion performance of PT under long-term exposure to seawater, from the perspectives of two crucial factors affecting the corrosion of NAB: corrosion time and PT concentration. Figure 3(a) illustrates Δm vs t curves in the presence and absence of different concentrations of PT. Table 3 presents the fitting results of mass loss variation with time based on a pseudo-first-order kinetic equation. In contrast to the blank, Δm of NAB in PT-containing solution slumps distinctly. Specifically, in the presence of 0.34 mmol/L PT, Δm decreases by 78.4% after 30 d of immersion. Moreover, the mass loss curves display a consistent download trend with increasing PT concentrations. As PT concentration escalates, Δm declines by 82.0%, 88.9%, 91.5% and 92.8%, respectively. Additionally, the degree of drop can be quantified using the IE (η_w) of PT, with all η_w data

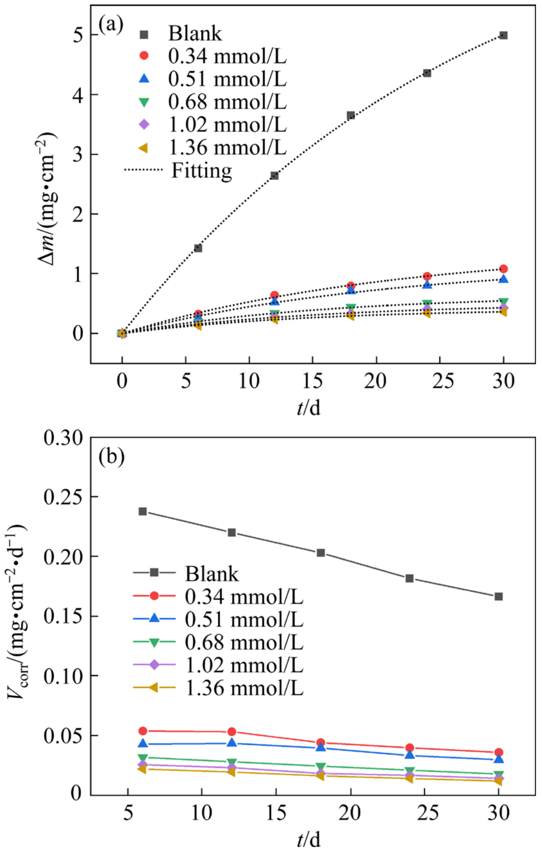

Fig. 3 Mass loss (a) and corrosion rate (b) of NAB in seawater without and with different concentrations of PT after different days immersion

from the mass loss experiment summarized in Table 4. As indicated in Table 4, the η_w of each group remains relatively constant after varying immersion time, and the maximum value reaches 92.8%. The stability of η_w suggests that the anti-corrosion effect of PT is highly dependable and exhibits excellent inhibitory properties. Additionally, corrosion rate curves (in Fig. 3(b)) show the similar regularity.

Table 3 Fitting parameters of mass loss curves

C/(mmol·L^{-1})	a	b	R^2
Blank	7.63	0.0355	0.9998
0.34	1.447	0.0454	0.9979
0.51	1.204	0.0465	0.996
0.68	0.6466	0.0618	0.9988
1.02	0.5057	0.0632	0.997
1.36	0.4204	0.0666	0.9993

a−Mass loss of NAB at equilibrium; b−Pseudo-first order rate constant

Table 4 IE from mass loss measurement with different concentrations of PT (%)

t/d	C/(mmol·L^{-1})				
	0.34	0.51	0.68	1.02	1.36
6	77.3	81.4	86.6	89.2	90.7
12	75.8	80.2	87.2	89.4	91.1
18	78.3	80.5	87.9	90.9	92.0
24	78.1	81.6	88.4	90.7	92.2
30	78.4	82.0	88.9	91.5	92.8

The change of the mass loss over time demonstrates a characteristic consistent with pseudo-first order kinetics, indicating a non-linear relationship between Δm and t. For instance, at a concentration of 0.34 mmol/L, the values of Δm after 6, 12 and 30 d are 0.3235, 0.6397 and 1.0801 mg/cm^2, respectively. This observation highlights that Δm after 12 d is 1.98 times greater than that after 6 d, while that after 30 d is 3.34 times larger than that after 6 d, in contrast to the theoretical expectation of a 5-fold increase. The results reveal that PT is qualified of excellent effect of anti-corrosion, and a stable barrier can be established on the PT/NAB interface.

3.2 Electrochemical impedance spectroscopy (EIS) analysis

To understand the intricate interfacial dynamics occurring on the surface of NAB with systems (NAB/PT/seawater) containing different concentrations of PT, the EIS was carried out at a stable state of the OCP. The Nyquist diagrams for NAB in seawater without and with different concentrations of PT at 303 K (2 h of immersion) are demonstrated in Fig. 4(a$_1$, a$_2$). Remarkably, the Nyquist plots with concentrations ranging from 0.34 to 1.36 mmol/L show a flat arc consisting of a depressed semi-circle in the high-frequency region (HF) and a significantly elongated loop in the low-frequency region (LF). This intriguing pattern is attributed to the presence of double-layer capacitance and charge transfer impedance on the NAB/seawater interface. The HF semicircle reflects the electrochemical double-layer capacitance, while the LF semicircle signifies the transfer of PT molecules across the NAB/seawater interface. The straight line appearing in LF of the blank results from the diffusive process of a series of active species (Cl$^-$, CuCl complexes, dissolved oxygen, etc). Compared with the blank, the straight line with an inclination angle of about 45° in LF not only disappears in the Nyquist diagrams of each experimental group but also is replaced by an arc with a radius at least 20 times larger than that of the blank. To quantify the corrosion inhibition effect of PT on NAB, the EIS results can be fitted using the equivalent circuit of Fig. 4.

Solution resistance (R_s), charge transfer resistance (R_{ct}), the resistance of protective film formed on the copper surface from PT or corrosion products (R_f), warburg impedance (W) and the constant phase elements (CPE) (Q_1 and Q_2) are collected in Table 5. Q_1 and Q_2 are used to calculate film capacitance (C_f) and double-layer capacitance (C_{dl}), which is expressed as follows [39]:

$$C_i=(Y_{0i}R_i^{1-n_i})^{1/n_i} \tag{5}$$

The polarization resistance (R_p=R_f+R_{ct}) representing corrosion resistance of NAB increases with the rising concentration of PT: R_p of 0.36 mmol/L increases by 28.6 times in comparison to the blank and R_p of 1.36 mmol/L increases by 285.5 times, which indicates that increasing the concentration of PT is significantly conductive to greater resistance on NAB/solution interface. Additionally, the IE (η_z) of PT follows a parallel ascending trajectory in tandem with R_p with varying PT concentrations. The highest η_z of PT reaches 99.6% at a concentration of 1.36 mmol/L.

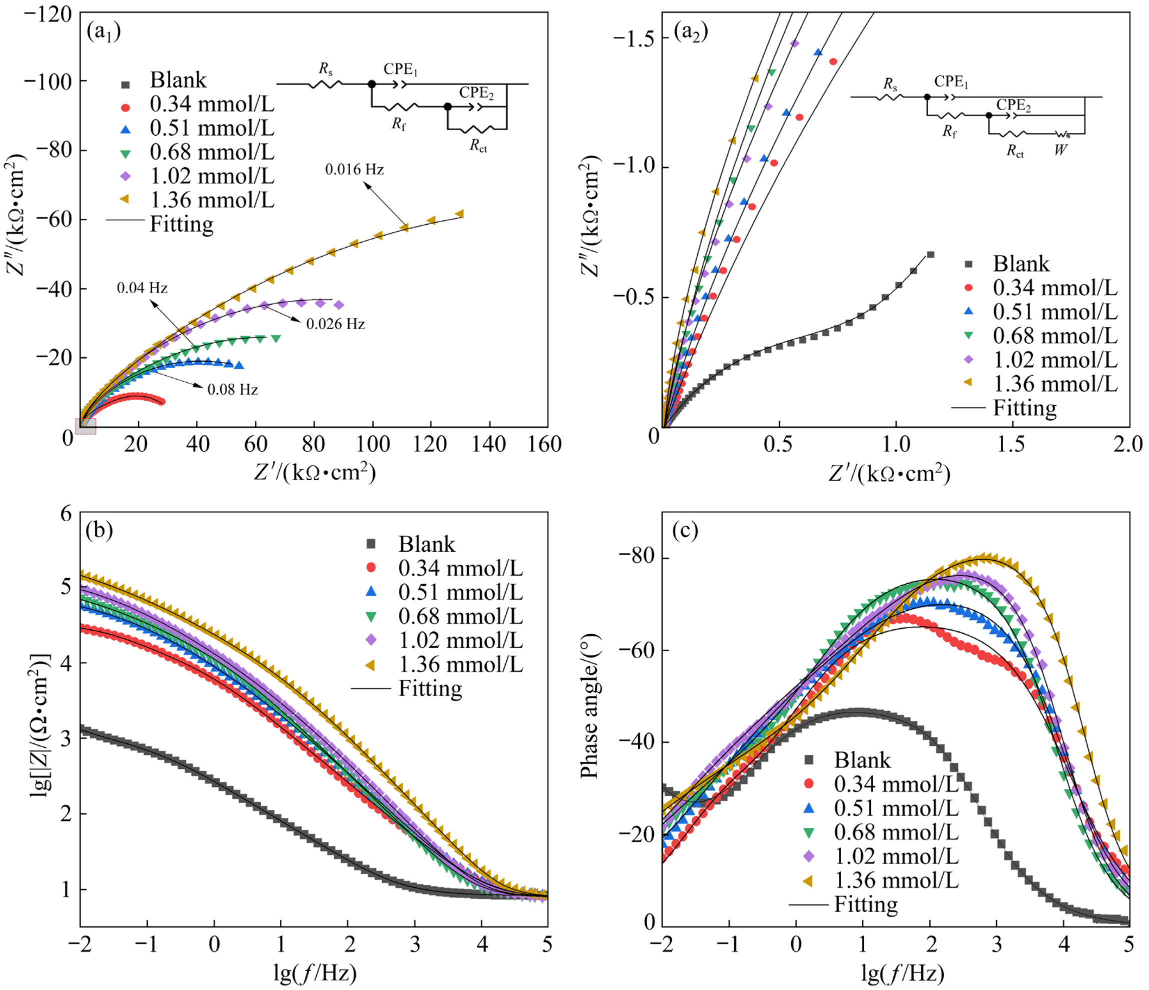

Fig. 4 EIS diagrams for NAB in seawater without and with different concentrations of PT: (a_1, a_2) Nyquist diagrams; (b) Bode diagrams; (c) Bode phase angle plots

Table 5 Impedance parameters obtained by fitting Nyquist plots with equivalent circuit

C/ (mmol·L^{-1})	R_s/ (Ω·cm^2)	R_f/ (Ω·cm^2)	Q_1: Y_1/ (Ω^{-1}·s^n·cm^{-2})	Q_1: n_1	C_f/ (μF·cm^{-2})	R_{ct}/ (Ω·cm^2)	Q_2: Y_2/ (Ω^{-1}·s^n·cm^{-2})	Q_2: n_2	C_{dl}/ (μF·cm^{-2})	w/ (Ω·cm^2)	η_z/%
blank	8.282	66.41	3.812×10^{-4}	0.7643	123	1149	8.203×10^{-4}	0.546	781	0.6717	
0.34	7.297	13606	3.049×10^{-5}	0.7496	22.7	21151	1.077×10^{-4}	0.6711	161		96.5
0.51	7.744	5086	1.454×10^{-5}	0.818	8.14	8.425×10^{4}	2.872×10^{-5}	0.4547	82.9		98.6
0.68	7.815	9060	1.048×10^{-5}	0.8712	7.4	1.229×10^{5}	3.182×10^{-5}	0.4611	157		99.1
1.02	7.9	2235	5.832×10^{-6}	0.9059	3.71	1.739×10^{5}	2.146×10^{-5}	0.4787	90		99.3
1.36	7.951	2425	1.985×10^{-6}	0.9411	1.42	3.446×10^{5}	1.525×10^{-5}	0.4405	125		99.6

From the perspective of the effect of the protective PT film on NAB, C_f and C_{dl} are considered [40]:

$$C_{dl}=\frac{\varepsilon^0\varepsilon S_e}{d} \tag{6}$$

$$C_f=\frac{F^2 S_e}{4RT} \tag{7}$$

where d is the thickness of the PT film, ε^0 is the permittivity in the vacuum, ε is the local dielectric constant, F is the Faraday's constant, R is the molar gas constant, and T is the thermodynamic temperature. The addition of PT contributes to a significant reduction in C_f and C_{dl}, indicating the considerable growth of the film on the

NAB/seawater interface. The more structured and denser barrier results from the firm adsorption of PT on the NAB surface.

Figures 4(b, c) illustrate relationship between lg f and lg $|z|$ and between lg f and the phase angle within the NAB/PT/seawater systems. In Fig. 4(b), the curve of the blank shows a valley related to a relaxation time constant in LF, indicating the presence of finite layer diffusion in LF. A peak appearing in HF suggests the presence of another time constant in the blank, correlated with charge transfer on the NAB surface. In contrast, the phase diagrams of the experimental systems reveal the presence of only one relaxation time constant. Remarkably, the peak value of phase angle in HF reaches approximately 80° at a concentration of 1.36 mmol/L, which reveals that the protective film on account of the successful adsorption of PT onto the NAB surface can effectively suppress the dissolution of metal ions (Cu^+, $AlCl_4^-$) on the NAB surface. Consequently, it blocks the formation of a diffusion layer for corrosive species, and this time relaxation constant is only related to the transfer of PT to NAB surface formation. Furthermore, the maximal phase angle of the experimental systems increases with the elevation of PT concentration, which further confirms the results obtained from the Nyquist plot. The EIS results demonstrate the excellent corrosion inhibition effect of PT on NAB in seawater.

3.3 Tafel curve analysis

The Tafel curves of the NAB specimen in PT-free and PT-containing seawater are shown in Fig. 5. The cathode curve in the blank is related to the dissolved oxygen in solution, while the anode curve fluctuates at −0.231 and 0.186 V. These fluctuations are attributed to the dissolution of metals on the NAB surface [41]. Upon the addition of PT at concentrations ranging from 0.34 to 0.68 mmol/L, the corrosion potential (φ_{corr}) shifts significantly in the direction of the anode. Concurrently, the corrosion current (J_{corr}) of the cathode and anode decreases. The trend indicates that the addition of PT at low concentrations can partially lead to the repression of the activation of Cu and Al dissolution and the reaction of dissolved oxygen. Therefore, PT is regarded as a mixed-type inhibitor. However, there are corners at about −60.7, −47.9, and −45.8 mV, in the anode branches of the Tafel curves. These features signify the continued presence of a diffusion process associated with the metal dissolution region at the metal/solution interface, despite the suppression of PT on J_{corr}. In contrast, the anode branches of Tafel curves of 1.02 and 1.36 mmol/L PT-containing systems express a smooth trend, suggesting that with an increase in PT concentration, the protective film formed by PT becomes denser. Thus, the performance of anti-dissolution of copper and aluminum is pronounced.

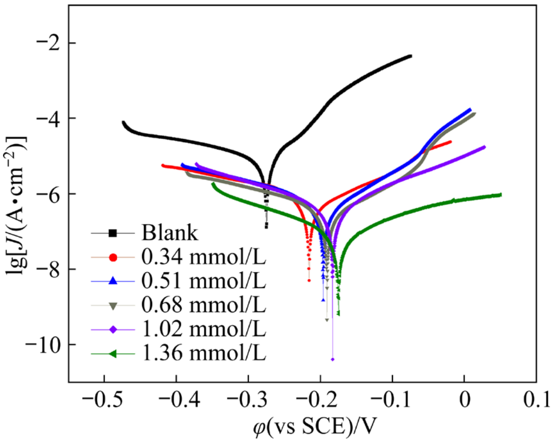

Fig. 5 Tafel polarization curves for NAB alloy in seawater without and with different concentrations of PT

The fitted parameters of the Tafel curve, including φ_{corr}, anode and cathodic Tafel slope (β_{a} and β_{c}), are summarized in Table 6. An analysis of these parameters shows that J_{corr} decreases dramatically compared to the blank and J_{corr} also decreases with the rise of PT concentration after adding PT to the corrosive medium. When the PT concentration is 1.36 mmol/L, J_{corr} decreases. Correspondingly, η_{i} increases from 93.8% to 99.5% with increasing the PT concentration. Besides, β_{c} and β_{a} show an increasing gradually but a downward trend, which indicates the slow decline of J_{corr} and the deepening anti-corrosion effect of PT on NAB. In details, owing to the protective compound formed by the chemical interaction between PT and NAB, the shape of anode branch related to NAB dissolution in inhibited medium is changed. On the cathodic curve, although the value of β_{c} decreases, its shape remains comparable to that of the blank, which suggests that the active site of the reaction process of O^2 to $OH^-$is reduced. Through the Tafel curve analysis, it is proven that PT is an organic molecule that is extremely helpful to NAB corrosion resistance.

Table 6 Tafel polarization parameters for NAB alloy in seawater without and with different concentrations of PMT

C/(mmol·L^{-1})	φ_{corr}(vs SCE)/V	J_{corr}/(A·cm^{-2})	β_a/(mV·dec^{-1})	β_c/(mV·dec^{-1})	Corrosion rate/(mm·a^{-1})	η_i/%
Blank	−0.2605	1.255×10^{-5}	56.72	−232.44	12.25×10^{-2}	
0.34	−0.2161	7.735×10^{-7}	113.2	−215.03	7.55×10^{-3}	93.8
0.51	−0.1961	4.122×10^{-7}	83.13	−153.8	4.02×10^{-3}	96.7
0.68	−0.191	2.632×10^{-7}	87.22	−148.5	2.57×10^{-3}	97.9
1.02	−0.1831	2.479×10^{-7}	110.3	−128.2	2.42×10^{-3}	98
1.36	−0.1749	5.691×10^{-8}	129.1	−118.8	5.55×10^{-4}	99.5

3.4 Adsorption isotherm

On account of the adsorption process of PT towards the NAB substrate, the NAB/seawater/PT system is characterized by the adsorption isotherm. The data of IE from electrochemical test are applied to estimating the surface coverage values (θ). The Langmuir adsorption isotherm as the optimal isotherm is utilized to fit the function of C/θ vs C, which can be expressed with the subsequent equation [42]:

$$C/\theta=1/K_{ads}+C \tag{8}$$

where C is the concentration of PT, and K_{ads} is the adsorption equilibrium constant.

The linearity of C/θ vs C from EIS is sketched in Fig. 6. The correlation (r^2) of the straight-line relationship is significantly above 0.999. Moreover, the adsorption free energy (ΔG^0_{ads}) can be determined by K_{ads} as follows [43]:

$$\Delta G^0_{ads}=-RT\ln(55.5K_{ads}) \tag{9}$$

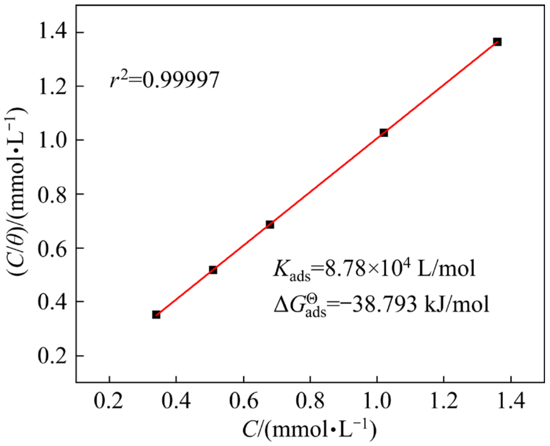

Fig. 6 Langmuir adsorption plot of NAB alloy based on data from EIS

The values of ΔG^0_{ads} obtained from the EIS is −38.793 kJ/mol. These results demonstrate that the adsorption of PT on the NAB/solution interface is a spontaneous process. Besides, it is worth noting that ΔG^0_{ads} value is between −20 and −40 kJ/mol, which manifests that PT is adsorbed on NAB substrate through both chem-adsorption and physical adsorption [44].

3.5 Surface morphology and characterization

3.5.1 SEM−EDS analysis

SEM−EDS analysis emerges as an effective method for confirming the excellent corrosion inhibition performance of organic molecules. SEM−EDS can analyze the morphology of NAB samples and the corresponding elemental content without and with the addition of 1.36 mmol/L PT. Figures 7(a_1, a_2, b_1, b_2) show the morphologies of NAB after 48 h immersion in uninhibited and inhibitive medium at 303 K. From the analysis of Fig. 7(a_1), a crack appears in the SEM image of the blank due to the attack from corrosive species such as Cl^- and OH^-. Conversely, under the protection of PT, there is little pitting or crack on the surface of NAB (Figs. 7(b_1, b_2)), suggesting explicit decrease of the corrosion degree. In the blank, some corrosion products accumulate on the NAB surface. Through EDS analysis, these corrosion products contain 14.6 wt.% O, and some trace elements (1.15 wt.% Cl). And the elemental contents of Cu and Al decline by about 32% and 7.4% compared to freshly abraded NAB. Meanwhile, only scratches abraded by 1200# sandpaper are found on the surface of the NAB specimen with PT. The EDS results show that the contents of Cu and Al elements are nearly the same as those of the untreated NAB sample. However, the content of oxygen element is greatly reduced, indicating that the corrosion products on the NAB surface are greatly reduced after adding PT. Trace amounts of S (0.76 wt.%) are also detected, which is related to the presence of sulfhydryl groups (—SH) in the PT structure.

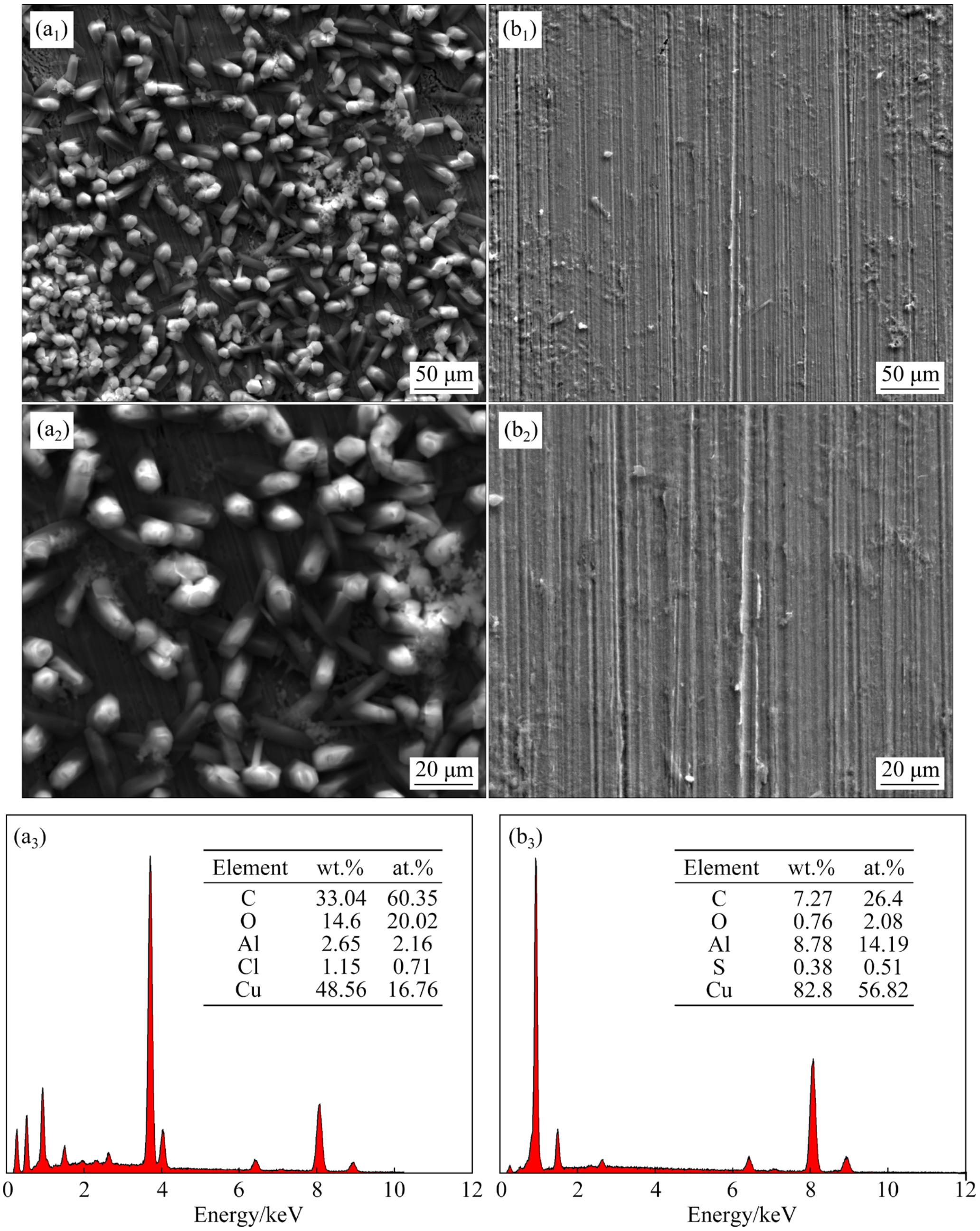

(a3)

Element	wt.%	at.%
C	33.04	60.35
O	14.6	20.02
Al	2.65	2.16
Cl	1.15	0.71
Cu	48.56	16.76

(b3)

Element	wt.%	at.%
C	7.27	26.4
O	0.76	2.08
Al	8.78	14.19
S	0.38	0.51
Cu	82.8	56.82

Fig. 7 SEM images and EDS results of NAB alloy after 48 h immersion in seawater at 303 K: (a_1−a_3) Blank; (b_1−b_3) With 1.36 mmol/L PT

3.5.2 Hydrophobicity of NAB surface

To offer additional verification of the film-forming property of PT on the NAB/PT interface, the WCA test was carried out. Figure 8 illustrates the morphologies of water droplets on the NAB surface with and without PT. The WCAs of three different positions on the surface of each NAB sample was measured for the assurance of experimental reliability. The WCA values for the untreated surface range from 31.3° to 35.1°, with a maximum value of 34.8°. In contrast, the PT-induced chemisorbed film exhibits remarkable hydrophobicity, with the highest WCA reaching 116.2°.

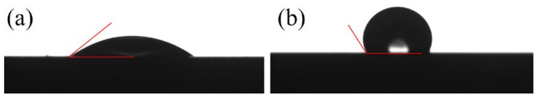

Fig. 8 Water contact angle (WCA) of NAB specimens after 6 h immersion in seawater at 303 K: (a) Blank; (b) With 1.36 mmol/L PT

3.5.3 AFM analysis

Figure 9 presents the 2D and 3D topographs of the NAB obtained by the AFM testing after 48 h

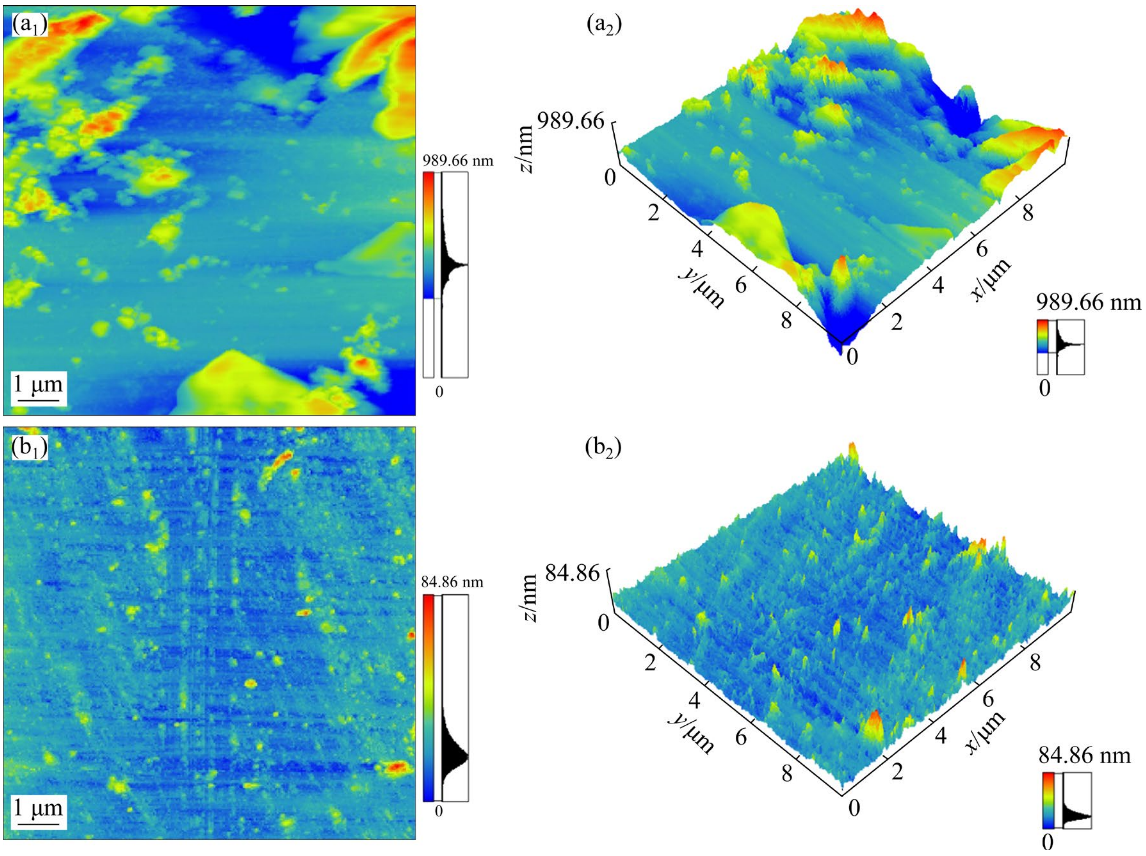

Fig. 9 AFM images of NAB specimens after 48 h immersion in seawater at 303 K: (a) Blank; (b) With 1.36 mmol/L PT

immersion in seawater with 1.36 mmol/L PT and without PT, with a selected area size of 10 μm × 10 μm. From Fig. 9, it is evident that the 2D and 3D maps of untreated NAB show uneven morphology. In the blank, corrosion products accumulate on the surface of NAB, forming various-sized particles attached to the surface of NAB and generating some cracks, which contribute to surface roughness. Conversely, the 2D and 3D maps of the NAB specimen with addition of 1.36 mmol/L PT appear predominantly blue, indicating relative smoothness. The arithmetic mean deviation (R_a) of the blank is 114.915 nm, the maximum profile peak height (R_p) reaches 697.76 nm, and the maximum profile valley depth (R_v) plunges to 916.248 nm. These values digitally prove the existence of cracks and the accumulation of surface corrosion products of NAB in the blank solution. In PT-containing solution, R_a, R_p and R_v are 4.905 nm, 64.378 nm and 20.493 nm, respectively, indicating the absence of obvious corrosion behavior on the NAB surface after the addition of PT to seawater.

3.5.4 XPS results of immersed NAB specimens

XPS analysis was performed to further explore the properties of the “film” formed on the PT/NAB interface and the chemical composition of NAB corrosion product. Figure 10 shows survey spectra and high-resolution spectra of NAB specimens after 48 h immersion at 303 K in seawater without and with the addition of 1.36 mmol/L PT. The high-resolution spectra of Cu 2p in different media are shown in Figs. 10(b, c). The peaks of Cu $2p_{1/2}$ and Cu $2p_{3/2}$ appear near the positions of (953.5±0.2) and 933.9 eV in both groups. In blank solution, however, there appears a satellite peak related to Cu(II) between Cu $2p_{1/2}$ and Cu $2p_{3/2}$ peaks [45]. The $Cu_2(OH)_3Cl$, and Cu(OH)Cl are detected in the Cl 2p spectra of the blank (Fig. 10(d)). Simultaneously, the peak of Cu_2O is located at 531.7 eV in O 1s spectra (Fig. 10(e)) [46]. The XPS analysis reveals that the corrosion products formed on NAB immersed in seawater for 48 h primarily consist of Cu(I) and Cu(II) compounds, including Cu_2O, and Cu(OH)Cl. Conversely, the peak related to corrosive product is not detected via XPS in the PT-containing solution. Some chemical bonds of PT appear in the O 1s spectrum (Figs. 10(f)): the positions of C—O, C═O and O—C═O peaks are

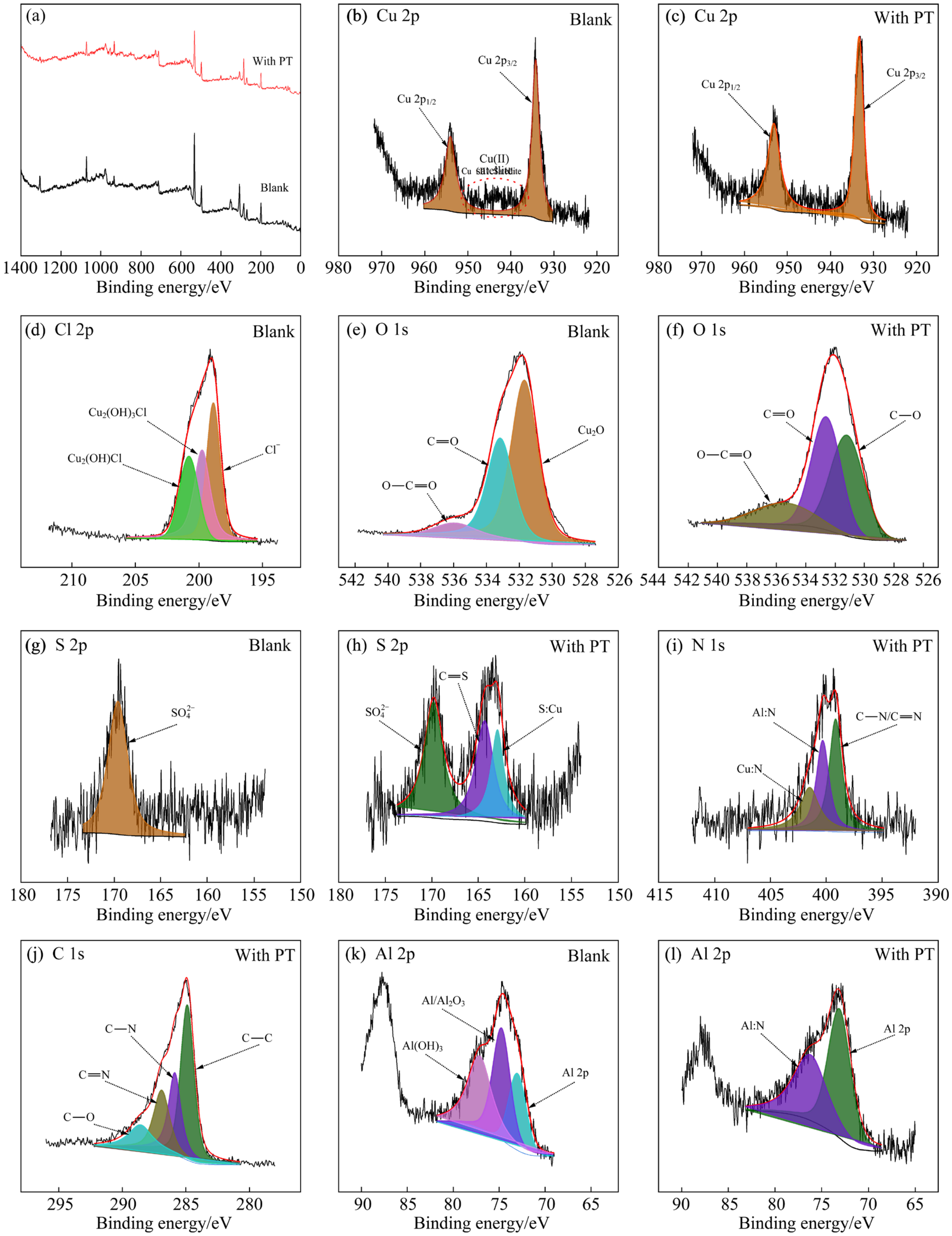

Fig. 10 XPS survey (a) and XPS high-resolution (b−l) spectra of NAB specimens after 48 h immersion in seawater with and without addition of 1.36 mmol/L PT at 303 K

at the binding energies of 531.2, 532.6, and 535.6 eV, respectively, where C—O is related to the chemical bond between C and O atoms on the pyrimidine ring of PT, while C═O and O—C═O can be ascribed to carbon pollution during the test (similar to the blank) [47]. The above results demonstrate a significant reduction in the corrosion products present on the NAB surface with the addition of PT.

Figures 10(f, g, h) can provide experimental evidence for the adsorption of PT on the NAB surface. Figure 10(h) shows the S 2p peak of NAB in PT-containing solution, where the peaks of C═S and S—Cu are detected at 164.4 and 162.8 eV, respectively. C═S is the chemical bond between the sulfhydryl group and the 6th carbon atom in PT, which indicates that PT can form a chemical adsorption with copper metal. Similarly, in blank solution, only SO_4^{2-} peak emerges from S 2p spectra, which is related to the presence of SO_4^{2-} in seawater. Figure 10(i) shows the N 1s peak of the experimental system. The surface of NAB exhibits the chemical bonds involving the metals Cu, Al and N atoms derived from the C—N and C═N bonds on the pyrimidine ring. In the C 1s (Fig. 10(j)) spectra, the C—C, C═N, C—N and C—O bonds from PT structure also appear on the surface of NAB in the PT-contained solution, which explains successful adsorption of PT on NAB surface [48]. The corrosion products of NAB contain Al_2O_3, and $Al(OH)_3$ in the blank [49] which can be seen from the Al 2p spectra (Figs. 10(k, l)). The Al—N bond at 76.3 eV in the experimental system indicates that the aluminum metal on the NAB surface can form chemical bonds with N atoms of PT molecule. In summary, the XPS analysis reveals that PT can form chemical complexes ($(PT—Cu)_{ads}$ and $(PT—Al)_{ads}$) with the metals of Cu and Al, respectively. These complexes can effectively protect NAB.

3.6 Distributions of HOMO and LOMO

Since the characteristics of the organic molecular structure are tightly related to the adsorption behavior of CIs on the metal surface, quantum chemical calculations have been utilized. Figure 11 presents the HOMO and LOMO distributions of PT. The HOMO electron clouds are primarily distributed on benzene ring in the presence of conjugated large π bond and LOMO is located on the N and S atoms within the pyrimidine ring. The HOMO and LOMO in organic structure represent the regions of the molecule providing electrons and accepting electrons, respectively.

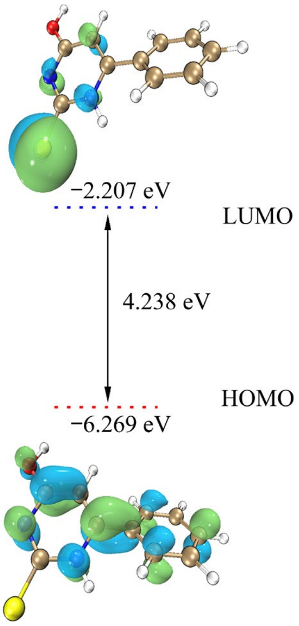

Fig. 11 Calculated molecular orbitals (LUMO and HOMO) and distribution of HOMO and LUMO of PT molecule

Besides, owing to the corrosion reaction in seawater, the Cu and Al are susceptible to generate unoccupied orbitals. Thus, the regions around N or S atoms show a greater tendency to be adsorbed on the surface of NAB. The calculated parameters including Δ*E*, electronegativity, global hardness and fractional electron tranfer (Δ*N*) are listed in Table 7.

3.7 Distributions of electrostatic potential (ESP)

The molecular electrostatic potential (MEP) mapping is able to distinguish nucleophilic and electrophilic sites in the iso-surface of ESP. Figure 12 clearly shows the distribution of electronic potential of PT. The red parts represent nucleophilic reaction sites while the blue are electrophilic attack sites. The locations and magnitudes of the extreme points are also presented in Fig. 12. The results of MEP mapping illustrate that the locations with high electronic density are predominantly centered around N and S atoms of pyrimidine ring, thereby facilitating the transfer with the NAB sheet. In combination to HOMO and LOMO distributions, S and N atoms are deemed as active adsorbed sites.

Table 7 Calculated quantum chemical parameters for PT

E_{HOMO}/eV	E_{LOMO}/eV	Δ*E*/eV	Electronegativity/eV	Global hardness/eV	Δ*N*/eV
−6.269	−2.207	4.062	4.238	2.031	0.146

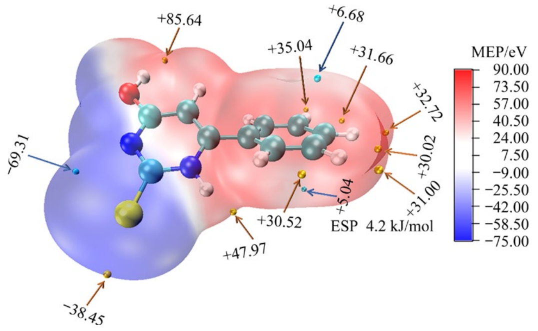

Fig. 12 Molecular electrostatic potential (MEP) mapping of PT molecular

3.8 Adsorption of PT on NAB surface by MD simulation

From the perspective of the adsorption behavior of PT, the MD simulation has been conducted to comprehensively investigate the interaction mechanism between NAB and PT. Figure 13 provides the top and side views of the adsorption configurations for PT on NAB matrix. It is evident that PT molecules are adsorbed on the NAB substate in the orientation of an approximate plane. Notably, S atom and N charge coordination bonds are closer to NAB surface. The interaction energy ($E_{\text{interatction}}$) and binding energy (E_{binding}) between PT and NAB can be summarized as

$$E_{\text{interaction}}=-E_{\text{binding}} \tag{10}$$

The binding energy is 59.73 kJ/mol, which induces the PT/NAB surface hard to supply a better corrosion resistance. The theoretical methods based on the MD simulation also indicate that the electronegativity around S or N atoms is closely correlated with high IE. This relationship is further confirmed by XPS test.

4 Discussion

4.1 Suppression of water molecules at different concentrations of PT

The H_2O phase is pivotal in the diffusion process on the PT/NAB interface. In order to estimate and simulate the suppression of PT on the diffusion of water molecules with different concentrations of PT, D_{i} has been applied to the explanation of the migration rate of corrosive ions. Figure 14 illustrates the variations of the diffusion models without and with PT molecules. As Fig. 14 indicates, PT molecules are more inclined to distribute around the NAB substrate, which is closer to real conditions. This distribution configuration of PT molecules can be considered as “PT film” on the NAB/seawater interface.

Figure 15 illustrates the variations of the MSD plots of H_2O particles at different concentrations of PT. In the blank, the calculated D_{i} of H_2O particles is $2.9906\times10^{-9}\,\text{m}^2/\text{s}$ which is close to the experimental data ($2.34\times10^{-9}\,\text{m}^2/\text{s}$) [37]. This exhibits the reliability of the diffusion calculation in this study. The addition of PT results in smaller slope of the H_2O MSD plots. When the number of PT molecules reaches 60, D_{i} (H_2O) is $1.1983\times10^{-9}\,\text{m}^2/\text{s}$ (drop by 60%), which shows that the “PT film” formed on the NAB surface can inhibit the migration of H_2O molecules. Moreover, the D_{i} of H_2O is diminished with the rising number of PT molecules, which theoretically elucidates that the corrosion effect of PT increases with the increase of the concentration of PT. More PT molecules concentrate to be absorbed on NAB

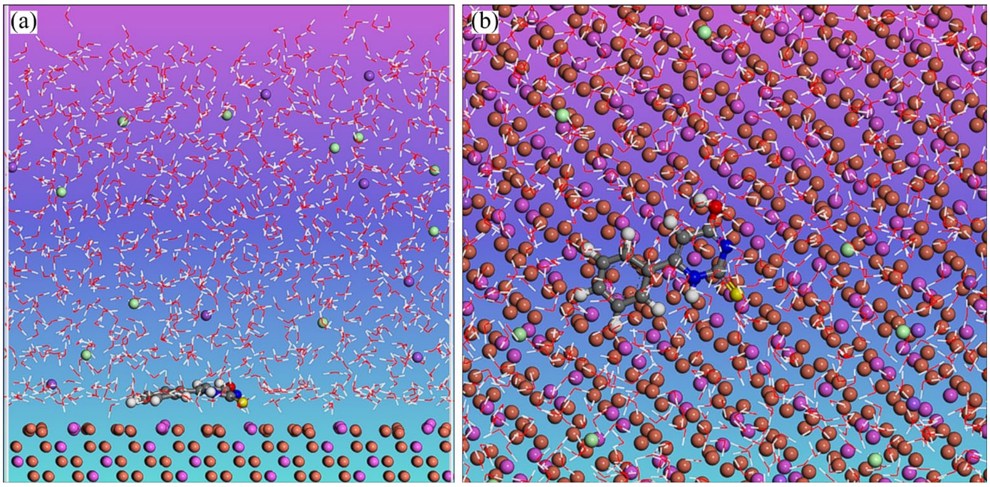

Fig. 13 Adsorption model of PT molecule on surface of NAB (110) after optimization: (a) Side view; (b) Top view

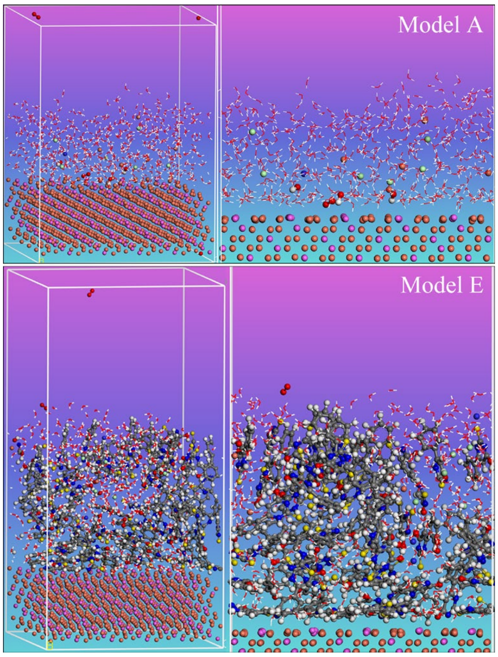

Fig. 14 Variations of diffusion models without and with PT molecules

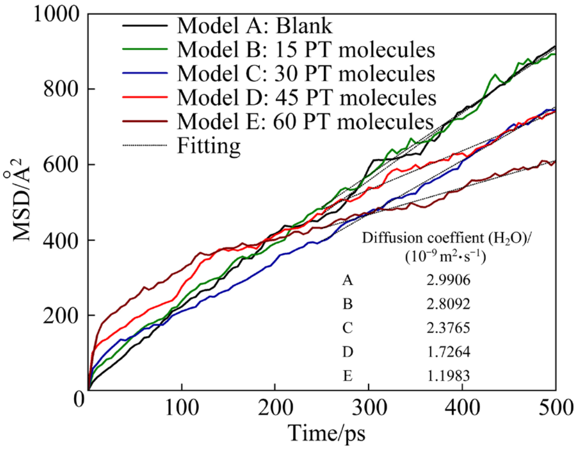

Fig. 15 MSD plots of H_2O particles in solution with different concentrations of PT at 303 K

matrix spontaneously, and they create a denser PT barrier. Consequently, the inhibition of the transfer of water phase particles such as H_2O between the H_2O phase and NAB matrix is enhanced. This result corroborates well with the regularity of experimental results.

4.2 Variations of corrosive species migration rates

The suppression of corrosive species presents a significant improvement with 60 PT molecules. Consequently, the diffusion process of other aggressive species including O_2, OH^-, Cl^-, Cu^{2+}, and Cu^+ is studied. Due to the conversion of the dissolved oxygen into OH^- during the corrosion process of NAB, both O_2 and OH^- particles are considered. With addition of 60 PT molecules, D_i of O_2 and OH^- shows a decrease of 95.9% and 79.8% compared with the blank, suggesting the significant decline of migration rate of O_2 and OH^-. This also theoretically implies the occurrence of cathodic electrochemical reaction related to dissolved oxygen on the NAB surface under the effect of PT. During the dissolution process of copper, Cu^+ and Cu^{2+} ions diffuse towards solution from the NAB substrate, which can also be repressed by PT molecules. The D_i of Cu^+ decreases from 0.123×10^{-9} to $0.0366\times10^{-9}\ m^2/s$ and that of Cu^{2+} is from 0.1603×10^{-9} to $0.0583\times10^{-9}\ m^2/s$. The PT barrier on the PT/NAB interface can extremely forbid the anodic reaction related to mental dissolution. The attack of Cl^- towards the NAB matrix is not to be neglected. The corresponding D_i decreases by 71.9%, which suggests that PT barrier prevents NAB from corrosion of Cl^-. The D_i values of corresponding species are listed in Table 8. The D_i values of O_2, OH^-, Cu^+, Cu^{2+} and Cl^- in PT-containing simulation model are markedly lower than those of the blank, which reveals that PT molecules can efficiently prevent the attack of corrosive ions on the NAB substrate.

Table 8 Diffusion coefficients (D_i) of various aggressive species in blank solution (Model A) and PT-containing solution (Model E)

Species	$D_i/(10^{-9}m^2\cdot s^{-1})$	
	Model A	Model E
H_2O	2.9906	1.1983
O_2	28.0642	1.1420
OH^-	0.1379	0.0279
Cu^{2+}	0.1230	0.0366
Cu^+	0.1603	0.0583
Cl^-	0.2817	0.0752

4.3 Mechanism of NAB corrosion and adsorption mechanism of PT

The mechanism of the NAB corrosion and the adsorption mechanism of PT on the NAB surface are sketched in Fig. 16. In seawater, the dissolution of the copper and aluminum always occurs originating from the attack of Cl^- ions (Fig. 16(b)).

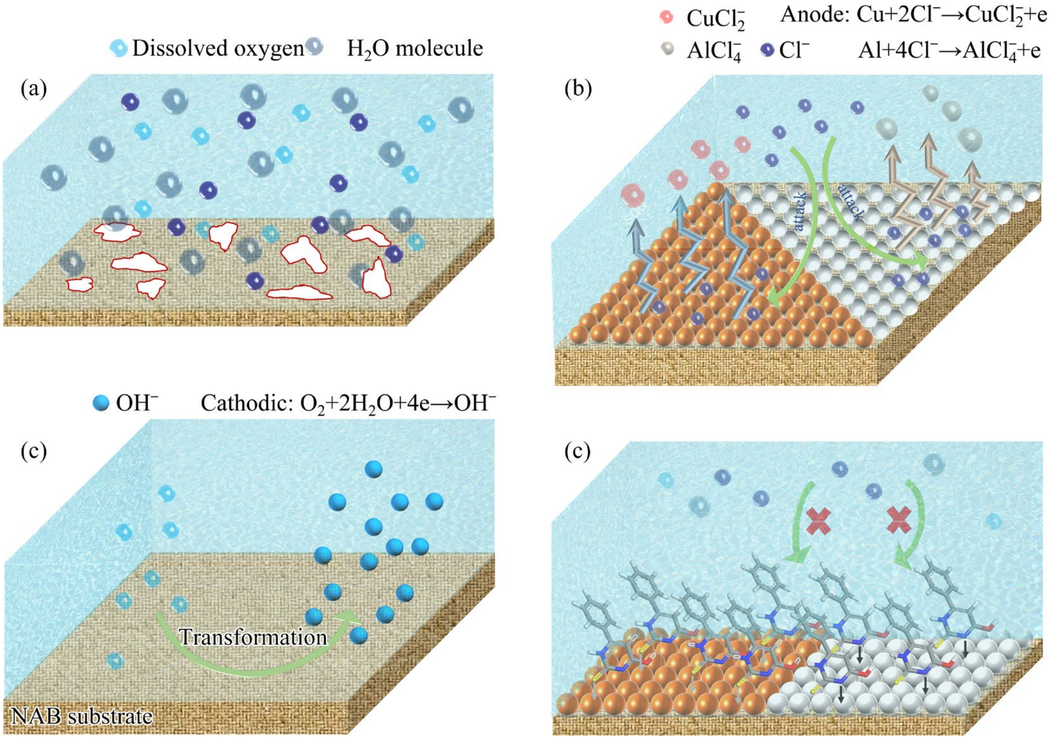

Fig. 16 Schematic of corrosion mechanism of NAB and adsorption mechanism of PT for NAB: (a) Blank; (b) Anodic reaction; (c) Cathodic reaction; (d) PT

The island-shaped corrosion products on the surface of NAB (Fig. 7(a)) are generated by the chemical interaction between the soluble $CuCl_2^-$, $AlCl_4^-$ ions and OH^-, which can be expressed as follows:

$$2CuCl_2^- + 2OH^- \rightarrow Cu_2O + H_2O + 4Cl^- \tag{11}$$

$$AlCl_4^- + 3OH^- \rightarrow Al(OH)_3 + 4Cl^- \tag{12}$$

The chemical composition of Cu_2O and $Al(OH)_3$ has also been confirmed by the results of XPS. The ultimate anti-corrosion effect is to eliminate the occurrence of above process. In theoretical calculation, these aggressive ions with high migration rate result in the corrosion on the NAB surface. With the addition of PT into the medium, the diffusion process of these species with lower D_i is significantly repressed. The degree of the NAB corrosion is greatly reduced and there is almost no corrosion phenomenon on the surface of NAB (Fig. 7(b)).

In the synthesis method, Position 6 of the 2-mercaptopyrimidine ring is modified by a benzene ring, so that the two six-membered rings form a bicyclic conjugated structure. The hydroxyl group modified at Position 4 of the pyrimidine ring greatly improves the solubility of PT in seawater. The protective film on the PT/NAB interface originates from the adsorption of PT, which is proven by near-flat orientation in MD calculation. Moreover, the S and N atoms in the pyrimidine ring are the active interaction sites. It is confirmed in XPS test. The denser PT film formed by the chemical reaction between PT and NAB is able to obtain batter suppression of the H_2O diffusion (Fig. 15), and the hydrophilicity on the NAB surface then decreases, which is consistent with experimental results (Fig. 8).

5 Conclusions

(1) PT exhibits higher inhibition performance than the most of pyrimidine inhibitors: the maximum IEs of PT reach 92.8% (η_w), 99.6% (η_z) and 99.5% (η_i) at a concentration of 1.36 mmol/L. The results of the 30 d mass loss experiment demonstrate that the IE of PT shows no decline trend, which suggests the high stability of PT film on the PT/NAB interface.

(2) Tafel curve analysis reveals that PT is a mixed inhibitor and the anode reaction is mainly affected in the inhibition of electrochemical reaction.

(3) The fitting result of the Langmuir isotherm model suggests that the adsorption belongs to physical and chemical adsorption. XPS, DFT and MD simulation reveal that PT molecules can be adsorbed on the NAB substrate with the active sites of N and S heteroatoms. S—Cu, Al—N and Cu—N bonds are formed by the chemical interaction between PT and NAB, which is proven through XPS. Thus, the adsorption of PT is mainly chemisorption.

(4) The diffusion of corrosive species is hindered considerably by the PT film with composition of $(PT—Cu)_{ads}$ and $(PT—Al)_{ads}$ on the PT/NAB interface. The degree of suppression is increased with the addition of more PT molecules.

CRediT authorship contribution statement

Jin-yu PI: Conceptualization, Methodology, Software, Formal analysis, Investigation, Data curation, Writing − Original draft; **Qi WANG:** Visualization; **Chao-yang FU:** Conceptualization, Methodology, Software, Investigation, Writing − Reviewing & editing, Supervision.

Declaration of competing interest

The authors declare that they have no known competing financial interests or personal relationships that could have appeared to influence the work reported in this paper.

Acknowledgments

This work was supported by the National Natural Science Foundation of China (No. 52171069). We also acknowledge the Analytical and Testing Center of Huazhong University of Science and Technology (China) for SEM measurements and the Center for Experimental Chemistry of Huazhong University of Science and Technology (China) for NMR spectroscopy.

Supporting Information

Supporting Information in this paper can be found at: http://tnmsc.csu.edu.cn/download/15-p0207-2023-0516-Supporting_Information.pdf.

References

[1] DING Yang, LV Yu-ting, ZHAO Bing-jie, HAN Yuan-fei, WANG Li-qiang, LU Wei-jie. Response relationship between loading condition and corrosion fatigue behavior of nickel-aluminum bronze alloy and its crack tip damage mechanism [J]. Materials Characterization, 2018, 144: 356−367.

[2] WHARTON J A, BARIK R C, KEAR G, WOOD R J K, STOKES K R, WALSH F C. The corrosion of nickel–aluminium bronze in seawater [J]. Corrosion Science, 2005, 47(12): 3336−3367.

[3] PARK K S, KIM S, Corrosion and corrosion fatigue characteristics of cast NAB coated with NAB by HVOF thermal spray [J]. Journal of the Electrochemical Society, 2011, 158(10): C335−C340.

[4] MOUSAVI S E, NAGHSHEHKESH N, AMIRNEJAD M, SHAMMAKHI H, SONBOLI A. Corrosion performance and tribological behavior of diamond-like carbon based coating applied on Ni−Al-bronze alloy [J]. Transactions of Nonferrous Metals Society of China, 2021, 31(2): 499−511.

[5] SONG Qi-ning, LI Hui-Lin, ZHANG Hao-nan, HONG Hao, XU Nan, ZHANG Gen-yuan, BAO Ye-feng, QIAO Yan-xin. Correlation between microstructure and corrosion and cavitation erosion behaviors of nickel aluminum bronze [J]. Transactions of Nonferrous Metals Society of China, 2022, 32(9): 2948−2964.

[6] LUO Qin, QIN Zhen-bo, WU Zhong, SHEN Bin, LIU Lei, HU Wen-bin. The corrosion behavior of Ni−Cu gradient layer on the nickel aluminum-bronze (NAB) alloy [J]. Corrosion Science, 2018, 138: 8−19.

[7] KEAR G, BARKER B D, STOKES K, WALSH F C. Flow influenced electrochemical corrosion of nickel aluminium bronze − Part I. Cathodic polarisation [J]. Journal of Applied Electrochemistry, 2004, 34(12): 1235−1240.

[8] CHEN Rui-ping, LIANG Ze-qin, ZHANG Wei-wen, ZHANG Da-tong, LUO Zong-qiang, LI Yuan-yuan. Effect of heat treatment on microstructure and properties of hot-extruded nickel-aluminum bronze [J]. Transactions of Nonferrous Metals Society of China, 2007, 17(6): 1254−1258.

[9] AL-HASHEM A, RIAD W. The role of microstructure of nickel–aluminium–bronze alloy on its cavitation corrosion behavior in natural seawater [J]. Materials Characterization, 2002, 48(1): 37−41.

[10] ZHANG Meng-han, LIU Shen-dan, JIANG Jing-yu, WEI Wei-chang. Effect of Cu content on intergranular corrosion and exfoliation corrosion susceptibility of Al−Zn−Mg−(Cu) alloys [J]. Transactions of Nonferrous Metals Society of China, 2023, 33(7): 1963−1976.

[11] LI Jian-yu, LÜ Shu-lin, CHEN Lu, LIAO Qiao, GUO Wei, WU Shu-sen. Influence of squeeze casting pressure on nanoparticle distribution and mechanical properties of nano-SiC_p/Al−Cu composites assisted with ultrasonic vibration [J]. Transactions of Nonferrous Metals Society of China, 2023, 33(7): 1977−1987.

[12] ZENG Si-qi, TIAN Jing-jing, HU Shu-bing, XIAO Ming, PENG Bo. Effect of laser surface melting on microstructure evolution and cavitation behavior of nickel aluminum bronze [J]. Transactions of Nonferrous Metals Society of China, 2023, 33(7): 2090−2109.

[13] SHAMSA A, BARKER R, HUA Y, BARMATOV E, HUGHES T L, NEVILLE A. Impact of corrosion products on performance of imidazoline corrosion inhibitor on X65 carbon steel in CO_2 environments [J]. Corrosion Science, 2021, 185: 16.

[14] LI Wei, TAN Bai-mei, ZHANG Shi-bao, GUO Lei, Jin-bo, YAN Mei, WANG Ru. Insights into triazole derivatives as potential corrosion inhibitors in CMP process: Experimental evaluation and theoretical analysis [J]. Applied Surface Science, 2022, 602: 154−165.

[15] KAYA S, KAYA C, GUO L, KANDEMIRLI F, TÜZÜN B, UĞURLU İ, MADKOUR L H, SARAÇOĞLU M. Quantum chemical and molecular dynamics simulation studies on inhibition performances of some thiazole and thiadiazole derivatives against corrosion of iron [J]. Journal of Molecular Liquids, 2016, 219: 497−504.

[16] PAUL P K, YADAV M. Investigation on corrosion inhibition and adsorption mechanism of triazine-thiourea derivatives at mild steel/HCl solution interface: Electrochemical, XPS, DFT and Monte Carlo simulation approach [J]. Journal of Electroanalytical Chemistry, 2020, 877: 114599.

[17] DOUCHE D, ELMSELLEM H, ANOUAR E H, GUO L, HAFEZ B, TÜZÜN B, EL LOUZI A, BOUGRIN K, KARROUCHI K, HIMMI B. Anti-corrosion performance of 8-hydroxyquinoline derivatives for mild steel in acidic medium: Gravimetric, electrochemical, DFT and molecular dynamics simulation investigations [J]. Journal of Molecular Liquids, 2020, 308: 113042.

[18] LUO Wei, LIN Qing-yun, RAN Xue, LI Wen-po, TAN Bo-chuan, FU An-qing, ZHANG Sheng-tao. A new pyridazine derivative synthesized as an efficient corrosion inhibitor for copper in sulfuric acid medium: Experimental and theoretical calculation studies [J]. Journal of Molecular Liquids, 2021, 341: 117370.

[19] REN Xiao-lei, XU Shen-ying, GU Xing-xing, TAN Bo-chuan, HAO Jiang-yu, FENG Li, REN Wei-hua, GAO Fang, ZHANG Shen-tao, XIAO Yi-ran, HUANG Lan. Hyperbranched molecules having multiple functional groups as effective corrosion inhibitors for Al alloys in aqueous NaCl [J]. Journal of Colloid and Interface Science, 2021, 585: 614−626.

[20] HASANIN M S, AL KIEY S A. Environmentally benign corrosion inhibitors based on cellulose niacin nano-composite for corrosion of copper in sodium chloride solutions [J]. International Journal of Biological Macromolecules, 2020, 161: 345−354.

[21] SHERIF E S M. Effects of 2-amino-5-(ethylthio)-1,3,4-thiadiazole on copper corrosion as a corrosion inhibitor in 3% NaCl solutions [J]. Applied Surface Science, 2006, 252(24): 8615−8623.

[22] ZHANG Q H, XU N, JIANG Z N, LIU H F, ZHANG G A. Chitosan derivatives as promising green corrosion inhibitors for carbon steel in acidic environment: Inhibition performance and interfacial adsorption mechanism [J]. Journal of Colloid and Interface Science, 2023, 640: 1052−1067.

[23] MOBIN M, ASLAM R, SALIM R, KAYA S, An investigation on the synthesis, characterization and anti-corrosion properties of choline based ionic liquids as novel and environmentally friendly inhibitors for mild steel corrosion in 5% HCl [J]. Journal of Colloid and Interface Science, 2022, 620: 293−312.

[24] HOU Bao-shan, ZHANG Q H, LI Y Y, ZHU G Y, LIU H F, ZHANG G A. A pyrimidine derivative as a high efficiency inhibitor for the corrosion of carbon steel in oilfield produced water under supercritical CO_2 conditions [J]. Corrosion Science, 2020, 164: 108334.

[25] YILDIZ R. An electrochemical and theoretical evaluation of 4,6-diamino-2-pyrimidinethiol as a corrosion inhibitor for mild steel in HCl solutions [J]. Corrosion Science, 2015, 90: 544−553.

[26] GUO W G, ZHAO J R, LI M, HU T, DAN Z Y Z, ZHANG Q, MA L Y, ZHANG S Y, ZHAO B Z. Design, synthesis and anti-tumor activity studies of novel pyrido[3, 4-d]pyrimidine derivatives [J]. Bioorganic & Medicinal Chemistry Letters, 2022, 76: 129020.

[27] XU Y, ZHANG S T, LI W B, GUO L, XU S Y, FENG L, MADKOUR L H. Experimental and theoretical investigations of some pyrazolo-pyrimidine derivatives as corrosion inhibitors on copper in sulfuric acid solution [J]. Applied Surface Science, 2018, 459: 612−620.

[28] SINGH A, ANSARI K R, CHAUHAN D S, QURAISHI M A, KAYA S. Anti-corrosion investigation of pyrimidine derivatives as green and sustainable corrosion inhibitor for N80 steel in highly corrosive environment: Experimental and AFM/XPS study [J]. Sustainable Chemistry and Pharmacy, 2020, 16: 100257.

[29] HEJAZI S, MOHAJERNIA S, MOAYED M H, DAVOODI A, RAHIMIZADEH M, MOMENI M, ESLAMI A, SHIRI A, KOSARI A, Electrochemical and quantum chemical study of Thiazolo-pyrimidine derivatives as corrosion inhibitors on mild steel in 1 mol/L H_2SO_4 [J]. Journal of Industrial and Engineering Chemistry, 2015, 25: 112−121.

[30] YADAV M, KUMAR S, SINHA R R, BAHADUR I, EBENSO E E. New pyrimidine derivatives as efficient organic inhibitors on mild steel corrosion in acidic medium: Electrochemical, SEM, EDX, AFM and DFT studies [J]. Journal of Molecular Liquids, 2015, 211: 135−145.

[31] GANDIN V, FERRARESE A, DALLA VIA M, MARZANO C, CHILIN A, MARZARO G. Targeting kinases with anilinopyrimidines: discovery of N-phenyl-N’-[4-(pyrimidin-4-ylamino)phenyl]urea derivatives as selective inhibitors of class III receptor tyrosine kinase subfamily [J]. Scientific Reports, 2015, 5(1): 16750.

[32] MURRAY K K, BOYD R K, EBERLIN M N, LANGLEY G J, LI L, NAITO Y. Definitions of terms relating to mass spectrometry (IUPAC Recommendations 2013) [J]. Pure and Applied Chemistry, 2013, 85(7): 1515−1609.

[33] LI X H, MU G N. Tween-40 as corrosion inhibitor for cold rolled steel in sulphuric acid: Weight loss study, electrochemical characterization, and AFM [J]. Applied Surface Science, 2005, 252(5): 1254−1265.

[34] MEHTA R K, GUPTA S K, YADAV M. Studies on pyrimidine derivative as green corrosion inhibitor in acidic environment: Electrochemical and computational approach [J]. Journal of Environmental Chemical Engineering, 2022, 10(5): 108499.

[35] SIN J, ARKHIPOV A, YIN Y, STONE J E, SCHULTEN K. Using VMD: An introductory tutorial [M]//Current Protocols in Bioinformatics. Hoboken, NJ: John Wiley & Sons, Inc., 2008.

[36] LU T, CHEN F W. Multiwfn: A multifunctional wavefunction analyzer [J]. Journal of Computational

Chemistry, 2012, 33(5): 580−592.

[37] HU S Q, GUO A L, YAN Y G, JIA X L, GENG Y F, GUO W Y. Computer simulation of diffusion of corrosive particle in corrosion inhibitor membrane [J]. Computational and Theoretical Chemistry, 2011, 964(1): 176−181.

[38] DOU F, HAN J, LI J H, ZHANG H X, QIAO K H, KAN J, CHEN J X. Exploration of novel polyaspartic acid derivatives as fluorescent eco-friendly corrosion inhibitors for the carbon steel: Electrochemical, surface analysis (SEM/XPS) and theoretical calculation [J]. Colloids and Surfaces A: Physicochemical and Engineering Aspects, 2023, 658: 130606.

[39] BRUG G J, VAN DEN EEDEN A L G, SLUYTERS-REHBACH M, SLUYTERS J H. The analysis of electrode impedances complicated by the presence of a constant phase element [J]. Journal of Electroanalytical Chemistry and Interfacial Electrochemistry, 1984, 176(1): 275−295.

[40] CHI B, LIN H, LI J B. Cations distribution of $Cu_xCo_{3-x}O_4$ and its electrocatalytic activities for oxygen evolution reaction [J]. International Journal of Hydrogen Energy, 2008, 33(18): 4763−4768.

[41] HAMMOUTI B, DAFALI A, TOUZANI R, BOUACHRINE M. Inhibition of copper corrosion by bipyrazole compound in aerated 3% NaCl [J]. Journal of Saudi Chemical Society, 2012, 16(4): 413−418.

[42] BENZBIRIA N, ECHIHI S, BELGHITI M E, THOUME A, ELMAKSSOUDI A, ZARROUK A, ZERTOUBI M, AZZI M. Novel synthetized benzodiazepine as efficient corrosion inhibitor for copper in 3.5% NaCl solution [J]. Materials Today: Proceedings, 2021, 37: 3932−3939.

[43] BELGHITI M E, BOUAZAMA S, ECHIHI S, MAHSOUNE A, ELMELOUKY A, DAFALI A, EMRAN K M, HAMMOUTI B, TABYAOUI M. Understanding the adsorption of newly benzylidene−aniline derivatives as a corrosion inhibitor for carbon steel in hydrochloric acid solution: Experimental, DFT and molecular dynamic simulation studies [J]. Arabian Journal of Chemistry, 2020, 13(1): 1499−1519.

[44] SUN Y H, ZHANG Y C, XU C, TAN B C, LI W P, ZHENG X W, BRAHMIA A. Honeysuckle extract as an environment-friendly corrosion inhibitor for copper in sulfuric acid medium [J]. Industrial Crops and Products, 2023, 197: 116551.

[45] ISMAIL K M. Evaluation of cysteine as environmentally friendly corrosion inhibitor for copper in neutral and acidic chloride solutions [J]. Electrochimica Acta, 2007, 52(28): 7811−7819.

[46] WANG Z Q, WANG X C, ZHANG S T, WANG Z Y, GAO F, LI H R. Simple and prompt protonation of new dyes containing double conjugated imine bonds to strengthen the protection of copper in aggressive sulfuric acid solution [J]. Journal of Molecular Liquids, 2021, 341: 117402.

[47] HUANG H J, FU Y, MU X J, LUO Z P, ZHANG S T, WANG Z Y, LI H R, GAO F. Molecular self-assembly of novel amphiphilic topological hyperbranched polymers for super protection of copper in extremely aggressive acid solution [J]. Applied Surface Science, 2020, 529: 147076.

[48] GAO L Z, PENG S N, HUANG X M, GONG Z L. A combined experimental and theoretical study of papain as a biological eco-friendly inhibitor for copper corrosion in H_2SO_4 medium [J]. Applied Surface Science, 2020, 511: 145446.

[49] CAI Xiang, YANG Meng-meng, WANG, Shuo, WANG Zan, ZHOU Jian, XUE Feng. Experimental investigations on corrosion behavior and antibacterial property of nickel-aluminum bronze fabricated through wire-arc additive manufacturing (WAAM) [J]. Corrosion Science, 2023, 214: 111040.

嘧啶衍生物作为镍铝青铜在海水中的环保型缓蚀剂

皮晋雨，王 琦，付朝阳

华中科技大学 化学化工学院 能源转换与存储材料化学教育部重点实验室
材料化学与服役失效湖北省重点实验室，武汉 430074

摘 要：合成嘧啶衍生物(6-苯基-2-硫脲嘧啶)作为一种缓蚀剂，应用于海水中镍铝青铜(NAB)的腐蚀防护。采用质量损失实验、电化学测试和表面分析方法评估了 6-苯基-2-硫脲嘧啶(PT)的缓蚀性能。结果表明，PT 表现出卓越的缓蚀效果，其最大缓蚀效率达到 99.6%。采用 X 射线光电子能谱和基于密度泛函理论的分子动力学模拟方法深入研究了 PT 的作用机制。S—Cu、Al—N 和 Cu—N 键的化学相互作用导致 PT 在 NAB 表面的吸附。由于保护性的 PT 膜$(PT—Cu)_{ads}$和$(PT—Al)_{ads}$在 PT/NAB 界面的形成，腐蚀物质的扩散受到了极大的抑制。随着 PT 分子的添加，抑制效果进一步加强。

关键词：镍铝青铜；缓蚀剂；扩散系数；吸附；海水

(Edited by Bing YANG)